

# Grid Connection Control of DFIG in Variable Speed Wind Turbines under Turbulent Conditions

Ahmed G. Abo-Khalil <sup>\*, \*\*, ‡</sup>

<sup>\*, ‡</sup>Department of Electrical Engineering, College of Engineering, Majmaah University, 11952, Saudi Arabia

<sup>\*\*</sup>Department of Electrical Engineering, Assuit University, Assuit, Egypt  
 (a.abokhalil@mu.edu.sa)

Received: 16.05.2019 Accepted: 26.06.2019

**Abstract-** Doubly-fed induction generators (DFIGs) are widely used in wind energy conversion systems. The dynamic features of DFIGs make it important to focus on designing high-performance control schemes. However, the dynamic characteristics of such generators depend on nonlinear parameters, such as stator flux, stator current, and rotor current, which increase overall system complexity. Therefore, robust controllers must be implemented with the ability to support the dynamic frequencies of wind energy to ensure system stability. Conventional vector control configurations that use proportional-integral controllers have various drawbacks, such as parameter tuning difficulties, mediocre dynamic performance, and reduced robustness. In this study, we focused on improving DFIG synchronization to the grid by applying Multi State Feedback (MSF) current controllers with a feedforward component to smooth the connection to the grid as well as to improve the steady-state and transient characteristics of the controller. MSF controllers are proposed to replace the proportional-integral controllers on both the rotor and grid sides. The proposed controller is designed using a multivariable system and feedforward control for input reference and incorporating disturbances into the control equations for fast synchronization and transient responses. To demonstrate the advantages of this controller, experimental studies are presented for both the transient and steady states.

**Keywords** DFIG, Synchronization, Rotor side converter, Grid side converter

## 1. Introduction

Doubly-fed induction generators (DFIGs) have been widely used in wind power generation since it has advantages such as high efficiency, quadruple active power, reactive power characteristics and small size power converter [1]. Moreover, the DFIG can maintain the constant system frequency regardless of the rotor speed, by the variable wind speed method. Unlike full converter wind turbine system with the same capacity of generators and converters, DFIG's converters account for 30% of the generator capacity. Because of these advantages, DFIG is the system type that occupies the largest portion of the wind turbine market at present. Currently, 50% of the wind energy market uses DFIG systems owing to their cost and size advantages [2], [3].

As shown in Figure 1, the stator of the generator is directly connected to the system and the rotor is connected to the two converters through the slip ring. Here, the converter connected to the rotor is referred to as a rotor side converter (RSC), and the converter connected to the grid is referred to as a system side converter (GSC). Until now, the controller method and performance evaluation of dual induction type wind turbine have been focused on the operation characteristics according to the slip of the generator. For example, the rotor effective power is transmitted from the stator to the grid when the generator slip is less than zero and to the opposite direction when greater than zero. Stator active

power and reactive power are controlled independently using stator flux reference [4]. For this reason, two converters are connected to the dc capacitor. The RSC independently controls the stator active and reactive power delivered to the grid to extract the maximum possible power from wind and enhance power quality through harmonic current filtering [5]–[10]. The RSC is also used to smooth stator synchronization with the grid. The main function of the GSC is to maintain a constant DC link voltage, regardless of power flow direction, and to control the magnitude and direction of rotor reactive power. The GSC is also used to remove reactive power pulsation under unbalanced conditions [11]–[14].

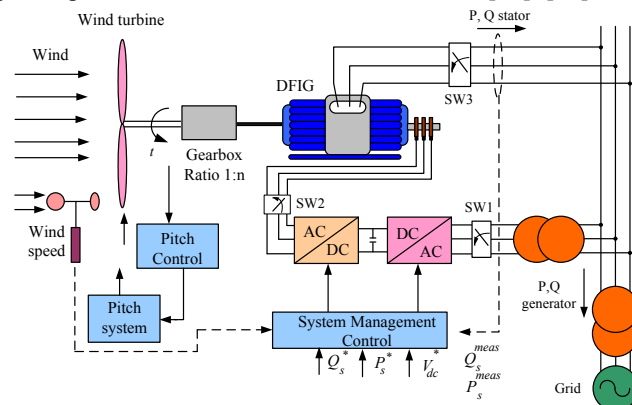


Fig. 1. Basic configuration of the proposed WECS.

Power converter performance largely depends on the accuracy of the implemented control strategy. Therefore, converter current controller performance is one of the most critical issues in power electronics circuits. The quality of a current controller can be evaluated based on several basic requirements [15]:

- 1 Over a wide output frequency range, both phase and amplitude errors should be zero.
- 2 The controller should have a fast-dynamic response.
- 3 The effects of load parameters changes should be compensated for.
- 4 Constant or limited switching frequencies should ensure reasonable lifetimes for power electronics semiconductor devices.
- 5 Total harmonic distortion should be minimized.

The current controller techniques listed in the literature can be divided into two main categories [16]–[18]: linear and nonlinear controllers. Proportional-integral (PI) stationary and synchronous, state feedback, and deadbeat controllers are examples of linear control techniques. These methods were introduced in [19] and [20].

The stationary PI technique has a major drawback in its inherent amplitude and phase error. To solve this problem and perform error compensation, several solutions have been proposed, such as using additional phase-locked loop (PLL) circuits [21] or feedforward correction [22]. However, when using a synchronous PI controller, the fundamental component error can be regulated to zero [22], but dynamic properties are still an issue.

Another well-known controller, namely the deadbeat controller, was designed to ensure strong dynamic responses [23]. The main advantages of this controller are that voltage measurements are not required to generate current references [24]. However, this controller suffers from a serious drawback in the form of inherent delays due to calculations. Furthermore, this controller does not include an integral control, which introduces steady-state errors.

The nonlinear controller category includes fuzzy logic controllers (FLC) and hysteresis controllers. A hysteresis current controller is typically implemented for the sake of simplicity. This method does not require any prior information regarding load parameters and has a fast response. However, based on a fixed hysteresis band, this current controller has a narrow band of switching frequencies for minimizing the peak-to-peak current ripple at all points of the fundamental frequency wave [25].

Another nonlinear controller, the FLC, is typically implemented as an alternative to a conventional PI compensator [26], [27]. For this controller, the design steps and controller accuracy depend on the knowledge and experience of the user.

In [28] and [29], a synchronization process with PI controllers are proposed which are used to compensate the magnitude and position of stator voltage. The using of several PI controllers lead to a slow dynamic response and difficulties in tuning the controllers' gains. In [30], the synchronization process is implemented using grid-flux oriented control, which is simulation for stator-flux oriented control algorithm. On the other hand, the power controller used the stator-flux oriented control. In this case, two control algorithms are used which make the implementation more complicated. In [31],

The stator active and reactive power are controlled separately by applying stator-flux oriented control. However, this paper hasn't discuss the synchronization process instead the DFIG is directly connected to the grid by starting up the DFIG as a motor which leads to the inrush current and poor power factor.

To compensate for these drawbacks, an MSF controller working with stationary or synchronous rotating coordinates can replace a conventional PI controller. In this controller, a feedback gain matrix can be calculated to ensure sufficient damping. Furthermore, an integral component can be added to minimize steady-state error to zero. Reference and disturbance inputs are used as feedforward signals and then added to the feedback control law to reduce transient error. The performance of the MSF controller has been discussed in a few papers, which have indicated superior performance compared to conventional PI controllers.

In this study, a dynamic model for DFIG systems and MSF control strategy for the RSC and GSC controllers were developed. To guarantee fast synchronization and robust steady-state control, MSF current controllers are proposed to replace the PI current controllers for both converters. To demonstrate the validity and exceptional performance of the proposed control algorithm, an experimental setup was designed and implemented. Finally, A comparison between the proposed method and a PI controller in the synchronization process is presented.

## 2. System Description

In DFIG-based WECSs, when ignoring the stator core and copper losses, all active and reactive power is supplied by both the stator and rotor. A maximum power point tracker is typically implemented to maximize the stator active power, which is extracted from the wind turbine. Regarding the rotor rotational speed, rotor power can be either supplied to or drawn from the grid depending on the operating speed. The grid feeds the rotor when the rotor rotates at sub-synchronous speeds and the rotor current lags behind the rotor voltage by less than 90°. At super-synchronous speeds, the rotor windings feed power to the grid and the rotor voltage jumps to nearly 180° ahead of the stator voltage, where the slip value is negative [32]–[33].

### 2.1. DFIG model

DFIG equations are similar to those for a squirrel-cage induction generator. The only modification to the equations is that the DFIG rotor terminals are not short-circuited. The model of a DFIG can be represented in a Park frame as [34]:

$$\begin{cases} v_{ds} = R_s i_{ds} + \frac{d\lambda_{ds}}{dt} - \omega_e \lambda_{qs} \\ v_{qs} = R_s i_{qs} + \frac{d\lambda_{qs}}{dt} + \omega_e \lambda_{ds} \\ v_{dr} = R_r i_{dr} + \frac{d\lambda_{dr}}{dt} - \omega_{sl} \lambda_{qr} \\ v_{qr} = R_r i_{qr} + \frac{d\lambda_{qr}}{dt} + \omega_{sl} \lambda_{dr} \end{cases} \quad (1)$$

where

$L_m$  : Magnetizing inductance;

- $L_s$  : Stator self-inductance;
- $L_r$  : Rotor self-inductance;
- $R_s$  : Stator resistance;
- $R_r$  : Rotor resistance;
- $\lambda_{dqs}$  : Stator dq-axis flux linkage;
- $\lambda_{dqr}$  : Rotor dq-axis flux linkage;
- $\omega_e, \omega_{sl}$  Synchronous and slip speed;
- $i_{dqs}, i_{dqr}$  : Stator and rotor dq-axis currents;
- $v_{dqs}, v_{dqr}$  : Stator and rotor dq-axis voltages.

The stator and rotor flux equations are as follows.

$$\begin{cases} \lambda_{ds} = L_s i_{ds} + L_m i_{dr} \\ \lambda_{dr} = L_m i_{ds} + L_r i_{dr} \\ \lambda_{qs} = L_s i_{qs} + L_m i_{qr} \\ \lambda_{qr} = L_m i_{qs} + L_r i_{qr} \end{cases} \quad (2)$$

In the case of stator-flux-oriented control, the stator flux angle is calculated from the flux components as follows:

$$\begin{cases} \lambda_{ds}^s = \int (v_{ds}^s - R_s i_{ds}^s) dt \\ \lambda_{qs}^s = \int (v_{qs}^s - R_s i_{qs}^s) dt \end{cases} \quad (3)$$

$$\theta_s = \tan^{-1} \frac{\lambda_{qs}^s}{\lambda_{ds}^s} \quad (4)$$

Then, the stator voltage is expressed as

$$v_{qs} = v_s \cdot \quad (5)$$

By ignoring the power losses, the active power can be written as a function of the d- and q-axis stator voltages and currents as follows:

$$P_s = \frac{3}{2} (v_{qs} i_{qs} + v_{ds} i_{ds}) = -\frac{3}{2} \cdot \frac{L_m}{L_s} \cdot v_{qs} i_{qr} \quad (6)$$

The reactive power is maintained at certain level by controlling the rotor d-axis current as:

$$Q_s = \frac{3}{2} (v_{qs} i_{ds} - v_{ds} i_{qs}) = \frac{3}{2} \cdot \frac{L_m}{L_s} \cdot v_{qs} (i_{ms} - i_{dr}) \quad (7)$$

If the magnitude of the magnetizing current  $i_{ms}$  is kept constant, d and q-axis currents can linearly regulate both active and reactive power. The control procedure for the RSC and GSC is detailed in the following section.

## 2.2. Rotor-side control

The kinematic energy of the wind passing through a rotating area of the blade can be calculated from [35]:

$$P_{wind} = \frac{1}{2} \rho A v^3 \quad (8)$$

Where  $A$  is the blade area [ $m^2$ ],  $\rho$  is the air density  $1.25$  [ $kg/m^3$ ], and  $v$  is the wind speed [ $m/s$ ].

This aerodynamic energy is expressed as kinetic energy according to the output coefficient ( $C_p$ ) in the blade as shown in Eq. (9).

The extracted power from the wind at any wind speed and turbine rotational speed is calculated as follows [36]:

$$P_{blade} = \frac{1}{2} \rho A v^3 C_p(\beta, \lambda) \quad (9)$$

The output coefficient ( $C_p$ ) is determined by the mechanical structure, such as blade length, pitch angle, and by the tip-ratio ( $\lambda$ ). The ratio is defined as the ratio of the wind speed to the blade rotational angular velocity as expressed as :

$$\lambda = \frac{\omega_m R}{v} \quad (10)$$

where  $\omega_m$  blade is the rotational angular velocity of the blade and  $R$  blade is the radius of the blade.

Figure 2(a) presents the turbine blade's variation with wind speed and rotational speed. At a particular rotational speed, the maximum power output occurs. Figure 2(b) shows the output coefficient ( $C_p$ ) varying with the main speed ratio ( $\lambda$ ). As the blade angular speed  $\omega_m$  increases, the output coefficient  $C_p$  increases, and when the specific reference value of the blade angular speed  $\omega_m$  increases, the output coefficient  $C_p$  decreases [37] – [39].

This  $C_p$  is variable depending on the design of the blade.  $C_p$  becomes the maximum value  $C_{p\_max}$  and the kinetic energy of the blade also has the maximum value when the principal speed ratio  $\lambda$  is the optimum value  $\lambda_{opr}$ .

Wind speed, blade angular velocity, and output coefficient curves are needed to implement the maximum output point tracking algorithm in wind power systems. The blade torque is expressed as [40] – [41]:

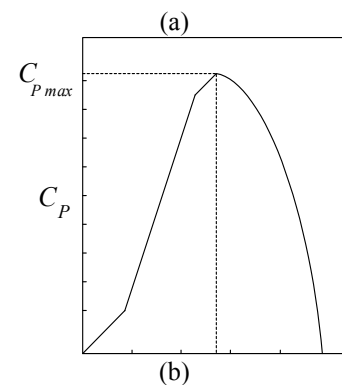
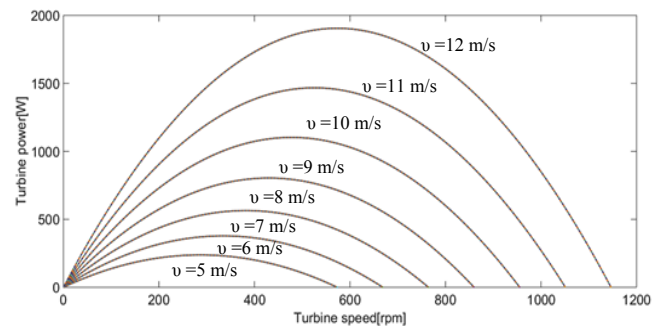


**Fig. 2.** Wind turbine characteristic curves: (a) wind turbine output power vs. rotational speed (b) power coefficient vs. tip-speed ratio

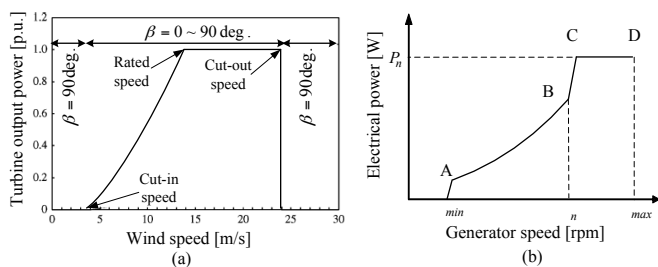


Fig. 3. Power curve in different modes.

The maximum power can be obtained by maintaining the relationship between the rotational speed and wind speed at its optimal value as:

$$\omega_{m,opt} = \lambda_{opt} \frac{v}{R} \quad (11)$$

The maximum power is then defined as

$$P_{max} = 0.5 \rho \pi R^2 C_{p,max} v^3 \quad (12)$$

The relationship between the turbine power and generator output power is calculated as

$$P_e = P_m - J \omega_m \frac{d\omega_m}{dt} - B_t \omega_m^2 \quad (13)$$

where  $P_e$  is the generator electrical power,  $J$  is the system moment of inertia,  $B_t$  is the friction coefficient, and  $\omega_r$  is the blade rotational speed.

The operating curve of the any wind turbine is depicted in Fig. 3. This curve can be divided into four regions as follows [42] – [43]:

- Region AB, when the wind speed is less than the cut in speed when the rotor is less than the minimum angular speed for optimum operation.
- Region BC, when the wind speed is higher than the cut-in speed and less than the rated value. The output power is given by  $P_{opt} = K_{opt} v^3$
- Region CD, when the rotational speed approaches to its rated value.
- Region DE, when the wind speed is beyond the limits and the generator output power is controlled to its rated value. The blade pitch controller is activated in this region.

The rotor reference q-axis current  $i_{qr}^*$  is then calculated as

the output of the active power controller and input for the inner current control loop. The rotor instantaneous q-axis current is then calculated from the sensed three-phase rotor currents and controlled to produce a reference q-axis rotor voltage. Similarly, a reference d-axis rotor voltage is produced by controlling the stator reactive power to the reference value. One can see how the outer stator power

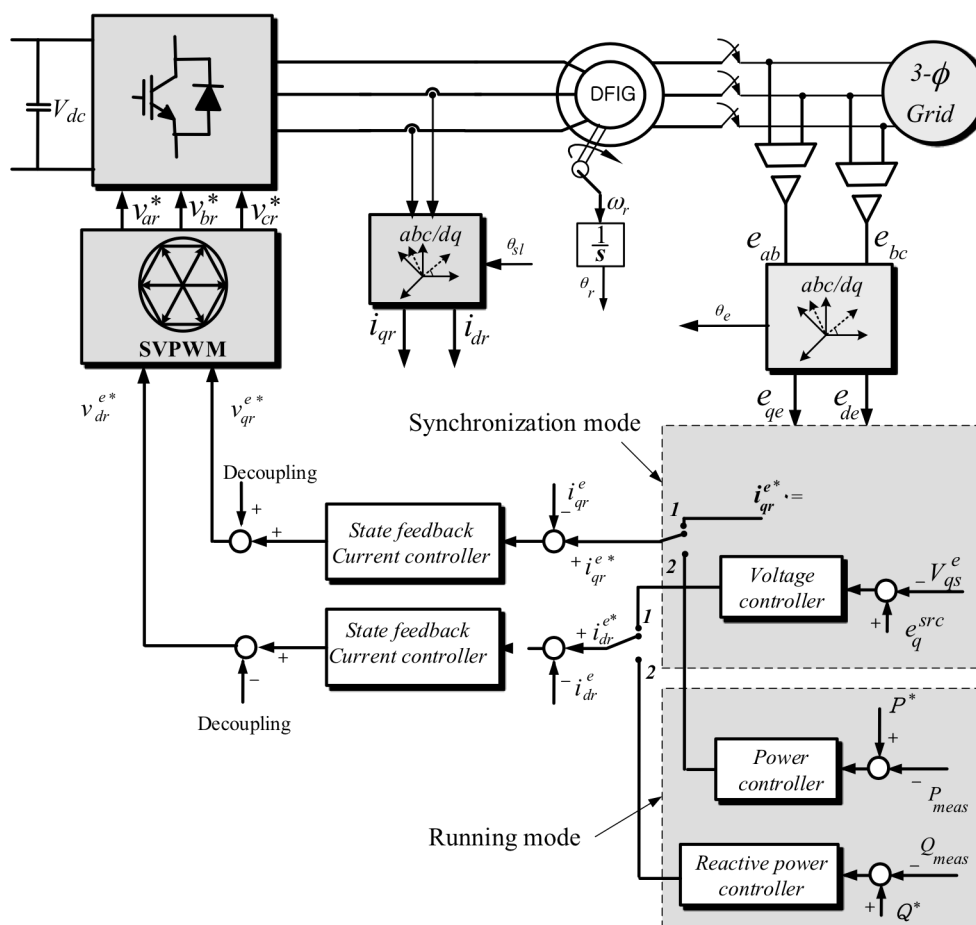


Fig. 4. Active and reactive power control for synchronization mode and running mode.

feedback loop produces the rotor reference d-axis current  $i_{dr}^*$  for the inner current feedback control loop. The reference q-axis rotor voltage is then produced by controlling the rotor d-axis component.

However, the DFIG synchronization mode control is different from the power mode control. To synchronize the DFIG with the grid, smooth connection of the DFIG to the grid is achieved when the stator voltage amplitude, frequency and phase are equal to the grid voltage are equal before closing the switch between the stator and the grid. The rotor side controller is activated to calculate the excitation current for the grid synchronization and power control loops as shown in Fig. 4. The excitation current generates the generator flux which builds-up the stator terminal voltages while the turbine accelerates until it reaches a certain value (e.g. 80% of the rated speed). At the same moment, the dc-link voltage in the bidirectional converter is soon charged. In addition, the stator frequency is almost the same as the grid and the stator voltage amplitude is also as the same as that of the grid. A phase-shift between the stator EMF and grid voltage may happen in case of slight difference in frequencies. To eliminate such phase shift, the phase difference compensation value  $\delta\theta_{sl}$  is determined and then added to the calculated slip angle [44]. By adjusting the stator d-axis voltage component to be zero which is the same value of the grid d-axis voltage, the compensation component  $\delta\theta_{sl}$  is determined.

Once this process is accomplished, the stator-side contactor is closed, and the generator is connected to the grid and then the power control mode starts. The optimum stator power is then calculated based on the wind speed and adjusted as the generator power reference. Figure 4 shows the the overall control system for both synchronization mode and running mode [44].

### 3. Grid-side Multivariable State Feedback Control

The goal of the GSC is to maintain a constant DC link voltage and boost it to a level that is higher than the amplitude of the line-line voltage. The DC link voltage is regulated to the reference value by using a PI controller. Any variation in the DC link voltage causes a change in the Q-axis reference current. The reactive power (or power factor) is controlled by using the D-axis reference current.

A state-space model for the converter can be obtained as

$$\dot{x} = Ax + Bu + Ed \tag{14}$$

$$y = Cx$$

(15)

where,

- $x$ : state vector;
- $\dot{x}$ : derivative of the space vector with respect to time;
- $u$ : input or control vector;
- $d$ : input disturbance vector;
- $y$ : output vector;
- $A$ : system matrix;
- $B$ : input matrix;
- $C$ : output matrix;
- $E$ : disturbance matrix.

Additionally,

$$x = \begin{bmatrix} i_{ds} \\ i_{qs} \end{bmatrix}, u = \begin{bmatrix} v_{dr} \\ v_{qr} \end{bmatrix}, d = \begin{bmatrix} e_{ds} \\ e_{qs} \end{bmatrix}$$

$$A = \begin{bmatrix} -\frac{R}{L} & \omega \\ -\omega & -\frac{R}{L} \end{bmatrix}, B = \begin{bmatrix} -\frac{1}{L} & 0 \\ 0 & -\frac{1}{L} \end{bmatrix}$$

$$E = -B, C = \begin{bmatrix} 1 & 0 \\ 0 & 1 \end{bmatrix},$$

where

- $e_s$ : source voltage;
- $i_s$ : source current;
- $v_r$ : converter input voltage;
- $R$ : line resistance;
- $L$ : boost inductor.

$\omega$  : the angular frequency of the source.

The state variables  $x$  are the source currents, the input vectors  $u$  are the converter input voltages in the DQ axis, the disturbance  $d$  is the source voltage in the DQ axis, and the output  $y$  is the equal to source current.

#### 3.1. State Feedback Control

Equations (14) and (15) define the state space model for any time-invariant linear multivariable system. When  $t \rightarrow \infty$ , the control target is [45]- [47]

$$\dot{x} \rightarrow 0 \text{ and } y \rightarrow y_r,$$

where  $y_r$  is a reference output.

Because MSF control is known to be a type of proportional control, the system performance in a steady state is inaccurate based on model uncertainty. This disadvantage can be overcome by introducing an integral control function to minimize steady-state error. The integral control function for the error  $p$  is defined as

$$p = \int_0^t (y - y_r) dt \tag{16}$$

Assuming that the reference output and disturbances are constant, substituting the derivative of (16) yields the following differential equations:

$$\dot{p} = y - y_r = Cx - y_r \tag{17}$$

By transforming these equations into matrix form, an augmented state model can be expressed as

$$\begin{bmatrix} \dot{x} \\ \dot{p} \end{bmatrix} = \begin{bmatrix} A & 0 \\ C & 0 \end{bmatrix} \begin{bmatrix} x \\ p \end{bmatrix} + \begin{bmatrix} B \\ 0 \end{bmatrix} u + \begin{bmatrix} E & 0 \\ 0 & -I \end{bmatrix} \begin{bmatrix} d \\ y_r \end{bmatrix} \tag{18}$$

In a steady state, the derivatives of the space vector and error approach zero because the disturbances and output references are assumed to be constant. Therefore, the steady-state solutions  $x_s$ ,  $p_s$ , and  $u_s$ , where the subscript ‘‘s’’ denotes a steady-state value, must satisfy the following equation:

$$\begin{bmatrix} E & 0 \\ 0 & -I \end{bmatrix} \begin{bmatrix} d \\ y_r \end{bmatrix} = -\begin{bmatrix} A & 0 \\ C & 0 \end{bmatrix} \begin{bmatrix} x_s \\ p_s \end{bmatrix} - \begin{bmatrix} B \\ 0 \end{bmatrix} u_s \tag{19}$$

Substituting (19) into (18) yields

$$\begin{bmatrix} \dot{x} \\ \dot{p} \end{bmatrix} = \begin{bmatrix} A & 0 \\ C & 0 \end{bmatrix} \begin{bmatrix} x - x_s \\ p - p_s \end{bmatrix} + \begin{bmatrix} B \\ 0 \end{bmatrix} (u - u_s) \quad (20)$$

To represent the deviations in these solutions from the steady state, a definition for new variables is introduced as follows:

$$z = \begin{bmatrix} z_1 \\ z_2 \end{bmatrix} = \begin{bmatrix} x - x_s \\ p - p_s \end{bmatrix} \quad (\dot{z} = \begin{bmatrix} \dot{x} \\ \dot{p} \end{bmatrix}), \quad (21)$$

$$v = u - u_s \quad (22)$$

Equation (22) can be defined in the standard state space equation as follows:

$$\dot{z} = \hat{A}z + \hat{B}v \quad (23)$$

where

$$\hat{A} = \begin{bmatrix} A & 0 \\ C & 0 \end{bmatrix}, \hat{B} = \begin{bmatrix} B \\ 0 \end{bmatrix}$$

The system in (23) is controllable when linear state feedback control can be applied. In such cases, the system can be expressed as follows:

$$\begin{aligned} v &= Kz \\ &= K_1z_1 + K_2z_2 \end{aligned} \quad (24)$$

where

$K$ : feedback gain matrix;  
 $K_1$  and  $K_2$ : partitioned matrices.

The partitioned matrices are derived via pole placement. By substituting from (24), (25), and (28), the control law is obtained as

$$u = K_1x + K_2p = K_1x + K_2 \int_0^t (y - y_r) dt \quad (25)$$

### 3.2. Feedforward Control

By using an integral controller, static errors can be regulated to be zero. However, system dynamic errors may be large during transients and disturbances. To reduce transient errors and the effect of disturbances, feedforward control can be used. To derive feedforward control equations, both reference inputs and disturbance inputs are used

The control system can be defined as follows:

$$\begin{bmatrix} \dot{x} \\ \dot{y} \end{bmatrix} = \begin{bmatrix} A & B \\ C & 0 \end{bmatrix} \begin{bmatrix} x \\ u \end{bmatrix} + \begin{bmatrix} E & 0 \\ 0 & -I \end{bmatrix} \begin{bmatrix} d \\ y_r \end{bmatrix} \quad (26)$$

The left-hand side of (26) becomes zero when the steady state reaches the steady-state condition. In this case,

$$\begin{bmatrix} x_s \\ u_s \end{bmatrix} = -\hat{G}^{-1}\hat{H} \begin{bmatrix} d \\ y \end{bmatrix} \quad (27)$$

where

$$\hat{G} = \begin{bmatrix} A & B \\ C & 0 \end{bmatrix}, \hat{H} = \begin{bmatrix} E & 0 \\ 0 & -1 \end{bmatrix}$$

The new relationship is the same and is defined as

$$u = K_1x + [-K_1 \quad I] \begin{bmatrix} x_s \\ u_s \end{bmatrix} \quad (28)$$

By substituting (28) into (25), we get

$$u = K_1x + K_{ff} \begin{bmatrix} d \\ y_r \end{bmatrix} \quad (29)$$

where the feedforward gain is defined as

$$\begin{aligned} K_{ff} &= [K_1 \quad -I] \hat{G}^{-1} \hat{H} \\ &= [K_{ff1} \quad K_{ff2}] \end{aligned}$$

The state variables, disturbances, and reference input equations comprise the total control equation, which is derived by substituting the integral control equation (16) into (29). The resulting control equation is written as follows:

$$u = K_1x + K_2 \int_0^t (y - y_r) dt + K_{ff} \begin{bmatrix} d \\ y_r \end{bmatrix} \quad (30)$$

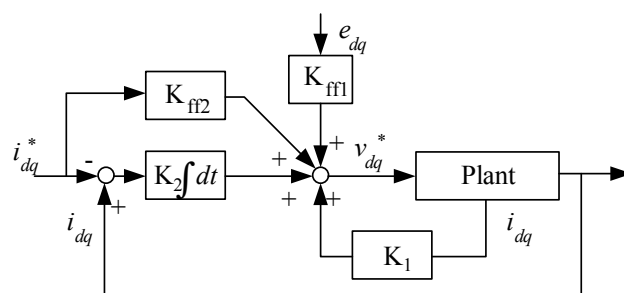


**Fig. 5.** Block diagram for MSF control with feedforward control

To illustrate the total control law in (30), a block diagram for the current controller, including the feedback and feedforward components, is presented in Fig. 5.

The feedback and feedforward controller components are depicted in Fig. 6. The actual DC link voltage is measured and compared to the voltage reference. The difference signal is then minimized by the DC link voltage controller. The output of the controller produces an inverter current reference in the d and q axes.

## 4. Experimental Results

Experiments were performed to study the performance of the multivariable state controller separately from the DFIG system. Several tests of the real operation of an insulated gate bipolar transistor (IGBT)-based PWM inverter in different conditions were conducted. It is desirable for the WECS to be implemented with hardware (motor-generator set) to test system operations in a laboratory. Figure 7 presents the hardware setup, which consists of a DFIG driven by a squirrel-cage induction motor as a wind simulator, back-to-back converters, and digital signal processor (TMS320C33) control boards.

In the first stage, the grid-side controller synchronizes the stator EMF and grid voltage by building up the stator EMF through the rotor d-axis current controller. The voltages phase difference between the two voltages is eliminated by using

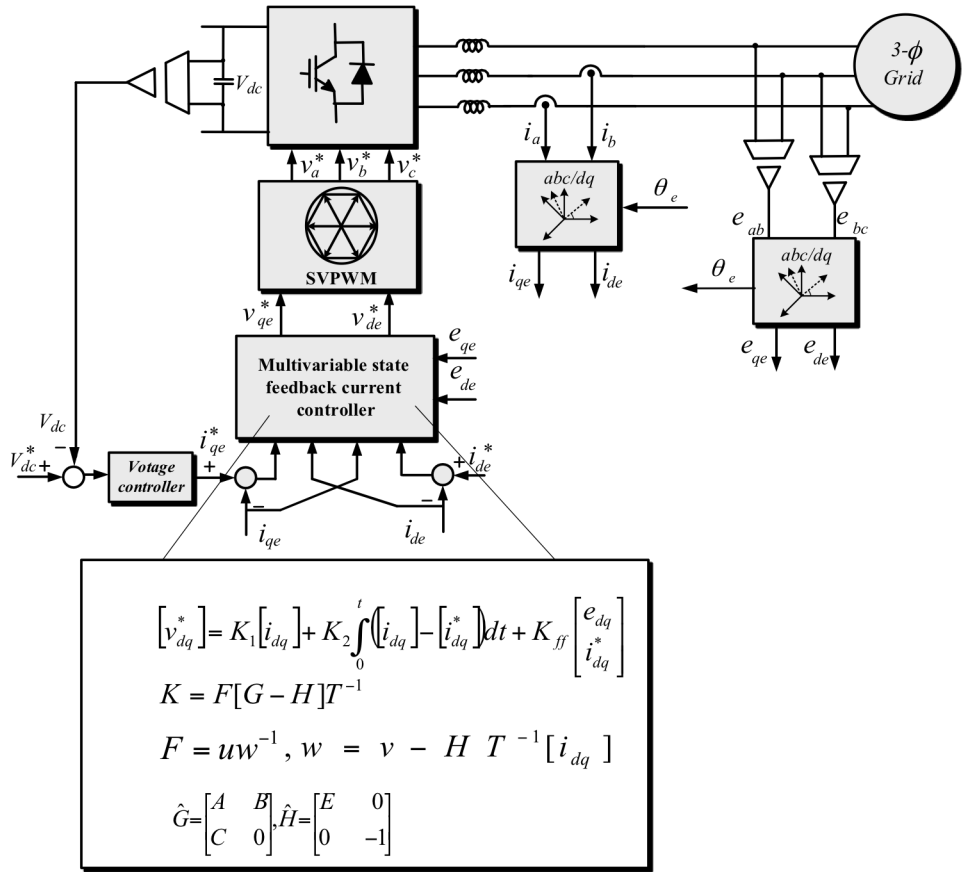


Fig. 6. Control block diagram for the PWM grid-side inverter.

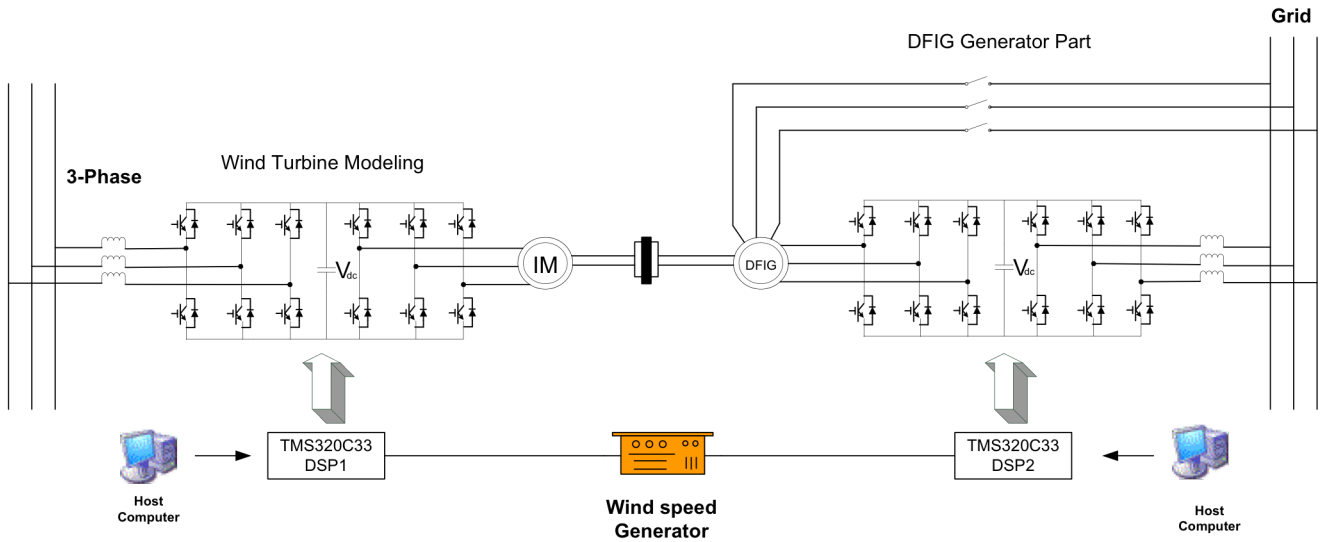
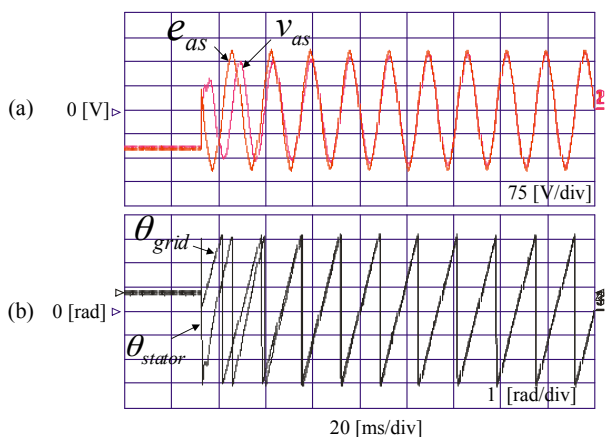


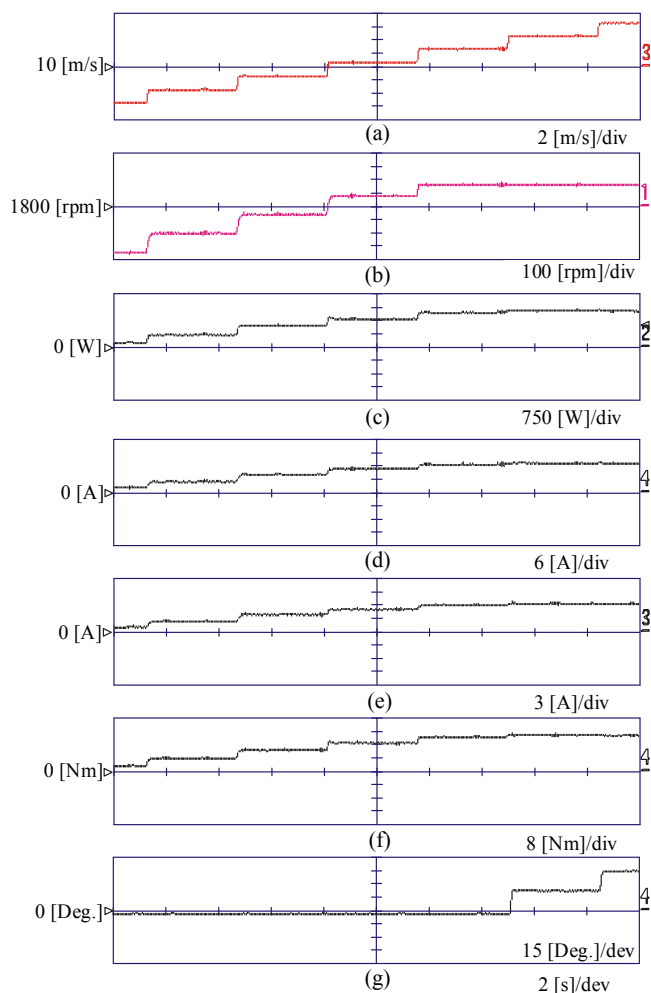
Fig. 7. Schematic of the experimental setup for a DFIG connected to the grid.

the PLL technique. The grid connection process can be achieved in less than two cycles.

Figure 8 (a) shows the connection process of a certain phase voltage of stator voltages with the corresponding phase of grid voltage. In the beginning, the stator EMF is zero then the rotor currents are controlled in order to build up the stator EMF in a fast and smooth way. In the same time, the phase difference between the EMF and grid voltages is eliminated as explained earlier.



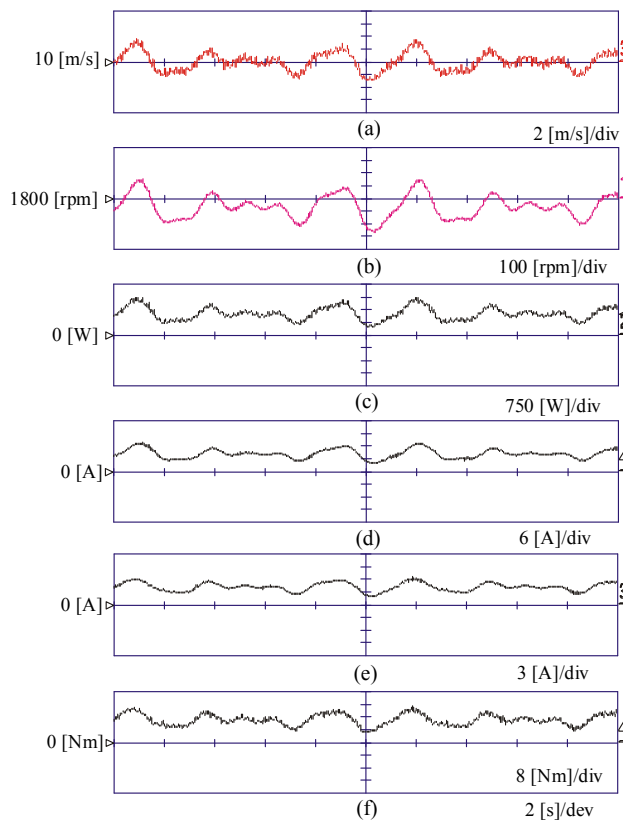
**Fig. 8.** Grid synchronization instant for state feedback controller: (a) stator and grid voltages, (b) stator and grid phase-angles



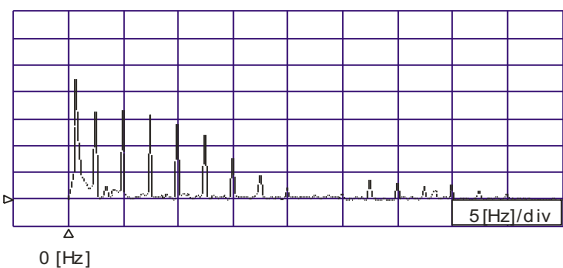
**Fig. 9.** Generator performance with step changes in wind speed: (a) wind speed, (b) Generator speed, (c) Generator output power, (d) rotor q-axis current, (e) Stator q-axis current, (f) generator electromagnetic torque, (g) Pitch angle.

Figure 9 presents the controller performance with step changes in wind speed. The wind speed increases in increments of 2 [m/s], starting from 5 [m/s]. For wind speeds less than 12 m/s, the pitch angle controller does not operate because the pitch angle is zero for the considered wind

turbine. The power controller controls the real power component to extract the maximum possible power. The power controller response at lower wind speeds is faster than the response at higher wind speeds. At wind speeds higher than 12 m/s, the pitch angle controller begins to operate to reduce the stress on the turbine blades.



**Fig. 10.** Generator performance with continuous wind speed variation: (a) wind speed, (b) Generator speed, (c) Generator output power, (d) rotor q-axis current, (e) Stator q-axis current, (f) generator electromagnetic torque.

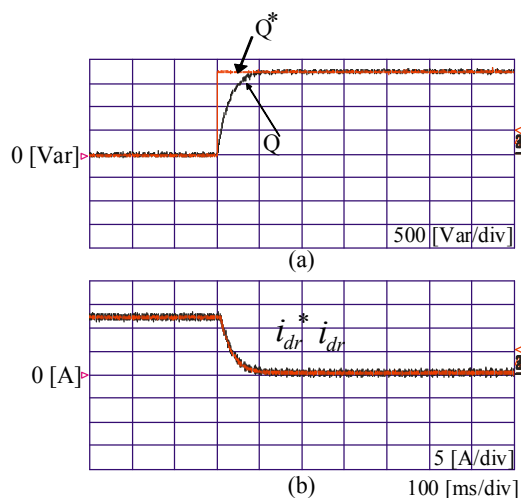


**Fig. 11.** Turbine torque spectrum.

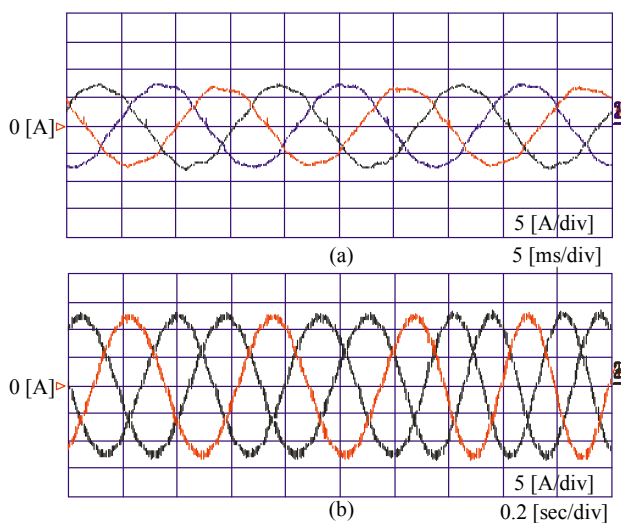
Next, we simulated the stochastic nature of real wind speeds. Figure 10 presents the DFIG parameters under turbulent wind speeds, where the mean wind speed is 10 m/s and the turbulence intensity is 20%. The active power changes when the wind is lower than 10 m/s, but it is maintained at the rated value when the wind speed increases beyond the rated value. The active power follows the wind speed pattern as shown in Fig. 10(c). Meanwhile, the rotor q-axis current component and generator torque follow the same pattern as shown in Figs. 10 (d) and (e).

Figure 11 shows the spectrum of the generator torque in Fig. 10(f). The 3p, 6p periodic components and its order are the dominant components that represents the frequencies of the wind shear and tower shadow components. It should be expected that the amplitude decreases when they increase in order.

To test the proposed controller performance, the stator reactive power reference changed in a step from 0 to 1750 Var as shown in Fig. 12. The actual reactive power follows the changes and the rotor d-axis current follows the reference as shown in Fig. 12 (a) and (b). The measured stator and rotor currents are depicted in Fig. 13 (a) and (b). It is obvious that the currents are almost sinusoidal. The spectrum shown in Fig. 14 indicates that the dominant frequency for the supply voltage and current is equal to the fundamental frequency 60 Hz.



**Fig. 12.** Reactive power control:  
 (a) stator reactive power and reference,  
 (b) rotor-side d-axis current and reference



**Fig. 13.** DFIG currents after synchronization:  
 (a) grid-side Q-axis current and reference,  
 (b) grid-side D-axis current and reference

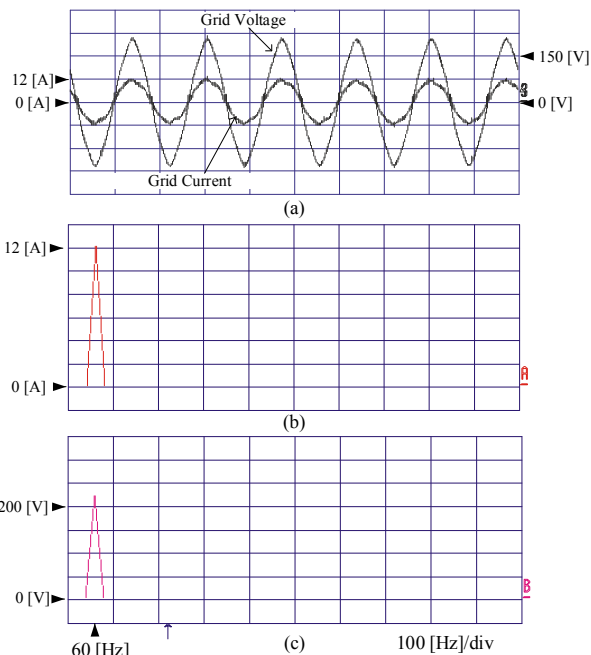


**Fig. 14.** (a) Steady-state waveforms of grid voltage and current  
 (b) Spectrum of grid current  
 (c) Spectrum of grid voltage

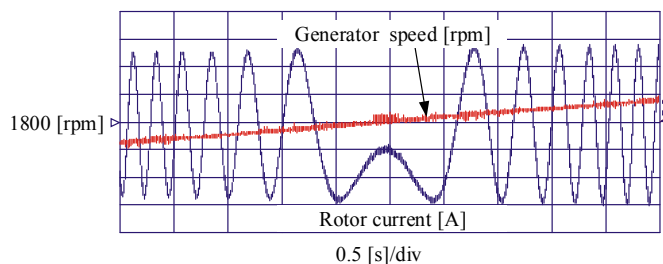


**Fig. 15.** Rotor current variation due to speed transition.

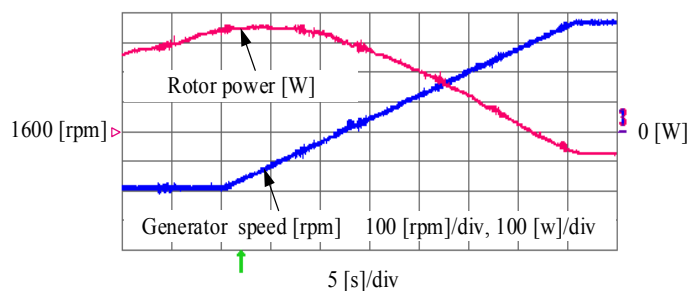


**Fig. 16.** Rotor power variation due to speed transition.

Figure 15 shows the rotor current variation from sub to super-synchronous speed. It is clear that the speed varies from sub to super-synchronous smoothly when a back-to-back converter is used. As the rotor speed increases, the rotor power decreases to zero and increases in the reverse direction. Theoretically, the rotor power reverse its direction at synchronous speed. However, the zero-crossing doesn't occur at the synchronous speed due to the different system losses such as rotor and converter losses. Figure 16 and 17 show that the zero-crossing is about 1875 rpm.

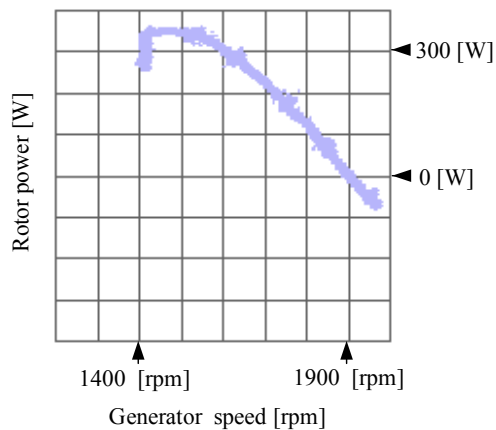


Fig. 17. Rotor power variation due to speed transition.

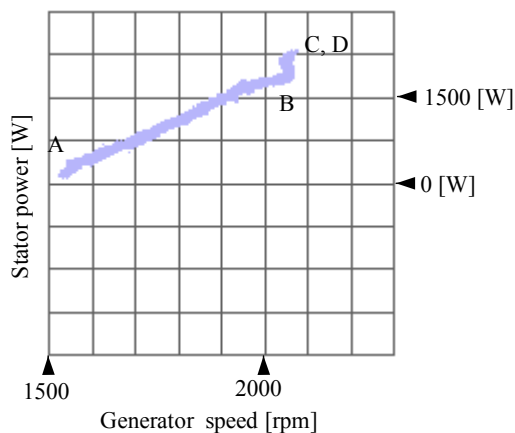


Fig. 18. Stator power variation due to speed transition

On the other hand, the power of the stator is optimized and controlled to track the maximum output for continuous wind speed variations. The region AB of Fig. 18 shows the maximum power tracking when the wind speed value is higher than the cut-in speed. When the generator rotational speed reaches its maximum value, the rotor speed is set to this value. Meanwhile the stator power increases whenever the wind speed increases as shown in Fig. 18. The pitch angle controller is activated when the wind speed increases over the pre-determined limit to maintain the output power at the rated value as described by the region DE.

### 5. Conclusion

This paper presented an MSF current controller for the RSC and GSC. The detailed design of the GSC controller was derived using the pole placement technique from multivariable system regulation theory. The GSC controller has two main parts: the outer DC link voltage controller, which is a PI controller, and the inner d- and q-axis current controllers, which are state feedback controllers. The outer voltage controller incorporating integral control regulates the DC link voltage with strong dynamics and zero steady state error. The inner current controllers guarantee fast transient responses and excellent dynamic performance. The RSC is controlled to extract the maximum possible power from wind

and to control the stator reactive power. The inner loops of the reactive and active power controllers are the d- and q-axis current controllers, respectively. Both current controllers use MSF to ensure excellent dynamic performance, which is necessary in the synchronization mode and control mode since the wind speed changes continuously and rapidly. For both the GSC and RSC, the control strategy is able to provide excellent performance under different operating conditions and shows the ability to connect the DFIG in about one cycle. This performance is achieved by using both feedforward and feedback components for the input references and disturbances.

### 6. References

- [1] A. G. Abo-Khalil, S. Alyami, K. Sayed, A. Alhejji, Dynamic Modeling of Wind Turbines Based on Estimated Wind Speed under Turbulent Conditions. *Energies*, Vol. 12, No. 10, 2019, pp. 1907.
- [2] Ahmed G. Abo-Khalil, H. G. Kim, D. C. Lee and J. K. Seok, Maximum Output Power Control of Wind Generation System Considering Loss Minimization of Machines, Proc. IECON'04, pp. 1676 - 1681, 2004.
- [3] M. Liserre, R. Cardenas, M. Molinas, et al, Overview of multi-MW wind turbines and wind parks, IEEE Transaction Industrial Electronics, Vol. 58, No. 4, 2011, pp. 1081–1095.
- [4] Ahmed G. Abo-Khalil, D. C. Lee, J. K. Seok, Variable Speed Wind Power Generation System Based on Fuzzy Logic Control for Maximum Output Power Tracking, Proc. Power Electronics Specialists Conference'04, pp. 2039-2043, 2004.
- [5] P. B. Eriksen, T. Ackermann, and H. Abildgaard, et al, System operation with high wind penetration, IEEE Power Energy Journal, Vol. 3, No. 6, 2005, pp. 65-74.
- [6] Ahmed G. Ab-Khalil, Control system of DFIG for Wind Power Generation Systems, LAP LAMBERT Academic Publishing, ISBN-10: 3659649813, ISBN-13: 978-3659649813, 2015.
- [7] E. Koutroulis and K. Kalaitzakis, Design of a maximum power tracking system for wind-energy-conversion applications, IEEE Trans. on Ind. Electr., Vol. 53, No. 2, 2006, pp. 486–494.
- [8] A. G. Abo-Khalil, Impacts of Wind Farms on Power System Stability, Intecopen, " In Muyeen, S.M., Al-Durra, A., Hasaniien, H.M. (eds.): Wind Farm'(InTechOpen, UK, 2013), ISBN 980–953–307–562–9, pp. 133–152.
- [9] H. Bekka, S. Taraft, D. Rekioua, S. Bacha, Power control of a wind generator connected to the grid in front of strong winds, Journal of Electrical Systems, Vol. 9, No. 3, 2013, pp. 267-278.
- [10] S. Taraft, D. Rekioua, D. Aouzellag, S. Bacha, A proposed strategy for power optimization of a wind energy conversion system connected to the grid. *Energy Conversion and Management*, Vol. 101, 2015, pp. 489-502.
- [11] R. Cardenas, R. Pena, S. Alepuz, et al., Overview of control systems for the operation of DFIGs in wind energy applications, IEEE Transaction Industrial Electronics, Vol. 60, No. 7, 2013, pp. 2776–2798.

- [12] G. Ramtharan, J. B. Ekanayake, and N. Jenkins, Frequency support from doubly fed induction generator wind turbines, *IET Renewable Power Generation*, Vol. 1, No. 1, 2007, pp. 3-9.
- [13] Ahmed G. Abo-Khalil and Hammad Ab-Zied, Sensorless Control for DFIG Wind Turbines Based on Support Vector Regression, *Industrial Electronics Conference IECON*, Canada, Oct. 2012.
- [14] Y. Song and H. Nian, Sinusoidal Output Current Implementation of DFIG Using Repetitive Control Under a Generalized Harmonic Power Grid With Frequency Deviation, *IEEE Trans. Power Electronics*, Vol. 30, No. 12, 2015, pp. 6751–6762.
- [15] M. P. Kazmierkowski L. Malesani, Current control techniques for three-phase voltage-source PWM converters: a Survey, *IEEE Transaction on Industrial Applications*, Vol. 45, No. 5, 1998, pp. 691-703.
- [16] F. Blaabjerg, R. Teodorescu, M. Liserre, A. V. Timbus, Overview of control and grid synchronization for distributed power generation systems, *IEEE Trans. Industrial Electronics*, Vol. 53, 2006, pp.1398–1409.
- [17] S. Xiao, H. Geng, H. Zhou, G. Yang, Analysis of the control limit for rotor-side converter of doubly fed induction generator-based wind energy conversion system under various voltage dips, *IET Renewable Power Generation*, Vol. 7, 2013, pp. 71–81.
- [18] M. Dai, M. N. Marwali, J.-W. Jung, A. A. Keyhani, A three-phase four-wire inverter control technique for a single distributed generation unit in island mode, *IEEE Trans. Power Electronics*, Vol. 23, 2008, pp. 322–331.
- [19] J. Rodriguez, J.-S. Lai, F. Z. Peng, Multilevel inverters: A survey of topologies, controls, and applications, *IEEE Trans. Industrial Electronics*, Vol. 49, 2002, pp. 724–738.
- [20] Q.-C. Zhong, J. Liang, G. Weiss, C. M. Feng, T. C. Green,  $H_\infty$  Control of the Neutral Point in Four-Wire Three-Phase DC–AC Converters, *IEEE Trans. Industrial Electronics*, Vol. 53, 2006, pp.1594–1602.
- [21] S.-K. Chung, Phase-locked loop for grid-connected three-phase power conversion systems, *Proc. Inst. Electr. Eng-Electron. Power Appl.*, Vol. 147, No. 3, 2000, pp. 213–219.
- [22] M. B. Delghavi, A. N. Yazdani, An adaptive feedforward compensation for stability enhancement in droop-controlled inverter-based microgrids, *IEEE Trans. Power Delivery*, Vol. 26, 2011, pp. 1764–1773.
- [23] Y. A. Mohamed, E. F. El-Saadany, An improved deadbeat current control scheme with a novel adaptive self-tuning load model for a three-phase PWM voltage-source inverter, *IEEE Trans. Industrial Electronics*, Vol. 54, 2007, pp.747–759.
- [24] X. Zhang, W. Zhang, J. Chen, D. Xu, Deadbeat control strategy of circulating currents in parallel connection system of three-phase PWM converter, *IEEE Trans. Energy Conversion*, Vol. 29, 2014, pp. 406–417.
- [25] N. Prabhakar, M. K. Mishra, Dynamic hysteresis current control to minimize switching for three-phase four-leg VSI topology to compensate nonlinear load, *IEEE Trans. Industrial Electronics*, Vol. 25, 2010, pp. 1935–1942.
- [26] H. Karim-Davijani, A. Sheikholeslami, H. Livani and M. Karimi-Davijani, Fuzzy logic control of doubly fed induction generator wind turbine, *World Applied Science Journal*, Vol. 6, No. 4, 2009, pp. 499-508.
- [27] J. Dannehl, C. Wessels, and F. W. Fuchs, Limitations of voltage-oriented PI current control of grid-connected PWM rectifiers with LCL filters, *IEEE Trans. Ind. Electron.*, Vol. 56, No. 2, pp. 380–388.
- [28] A. G. Abo-Khalil, D.-C. Lee, S. -H. Lee, Synchronization of DFIG output voltage to utility grid in wind power system, *IASTED conf proc in Rhodes*, pp.372-377, June. 2006.
- [29] A. G. Abo-Khalil, D. -C. Lee, S.-H. Lee, Grid Connection of Doubly-Fed Induction Generators in Wind Energy Conversion System, *Proc. of PEMC.2006, CES/IEEE 5th*, Vol. 3, pp. 1-5, Aug 2006.
- [30] G. Tapia, G. Santamara, M. Telleria, A. Susperregui, Methodology for Smooth Connection of Doubly Fed Induction Generators to the Grid”, *IEEE Transactions on Energy Conversion*, Vol. 24, No. 4, 2009, pp. 959-971.
- [31] R. Pena, J.C. Clare, and G. M. Asher, Doubly fed induction generator using back-to-back PWM converters and its application to variable speed wind-energy generation, *IEE Proc. Electr. Power Appl.*, Vol. 143, No. 3, 1996, pp. 231-241.
- [32] H.S. KO, Supervisory voltage control scheme for grid-connected wind farms, Ph.D. Dissertation, Dept. Elect. And Comp. Eng., Univ. of British Columbia, Vancouver, BC, Canada, 2006.
- [33] J. A. Baroudi, V. Dinavahi, A. M. Knight, A review of power converter topologies for wind generators, *Renew. Energy*, Vol. 32, 2007, 2369–2385.
- [34] Y. Song and H. Nian, Sinusoidal Output Current Implementation of DFIG Using Repetitive Control Under a Generalized Harmonic Power Grid With Frequency Deviation, *IEEE Trans. Power Electronics*, Vol. 30, No. 12, 2015, pp. 6751–6762.
- [35] H.G. Park, A.G. Abo-Khalil, D.C. Lee, K.M. Son, Torque ripple elimination for doubly fed induction motors under unbalanced source voltage. In *proceedings of the 2007 7th International Conference on Power Electronics and Drive Systems*, Bangkok, Thailand,; Vol. 7, pp. 1301–1306, November 2007.
- [36] A. G. Abo-Khalil, Model-based optimal efficiency control of induction generators for wind power systems, *ICIT 2011*, pp. 191-197.
- [37] M. Nadour, A. Essadki, T. Nasser, “Comparative Analysis between PI & Backstepping Control Strategies of DFIG Driven by Wind Turbine”, *International Journal of Renewable Energy Research (IJRER)*, vol. 7, no. 3, 2017.
- [38] M.B.C Salles, A.J.S Filho and A.P.Grilo, A Study on the Rotor Side Control of DFIG-based Wind turbine during Voltage Sags without Crowbar System, *International Conference on Renewable Energy Research and Applications, ICRERA*, 2013.
- [39] E.Aydin, A. Polat, L.T.E Ergene, Vector Control Of DFIG n Wind Power Application, *International Conference on Renewable Energy Research and Applications, ICRERA*, 2016.
- [40] M. Ferrari, GSC control strategy for harmonic voltage elimination of grid-connected DFIG wind turbine,

- International Conference on Renewable Energy Research and Applications, ICRERA, 2016.
- [41] A.G. Aissaoui, A. Tahour, M. Abid, N. Essounbouli, F. Nollet, Using Neuro Fuzzy PI Techniques in Wind Turbine Control, International Conference on Renewable Energy Research and Applications, ICRERA, 2013.
- [42] H. G. Park, A. G. Abo-Khalil, DC Lee, Wind turbine simulators considering turbine dynamic characteristics, The Transactions of The Korean Institute of Electrical Engineers, Vol. 57, No. 4, 2008, pp. 617-624.
- [43] A. G. Abo-Khalil, A new wind turbine simulator using a squirrel-cage motor for wind power generation systems, Power Electronics and Drive Systems (PEDS) Proc., pp. 750-755, 2011.
- [44] Ahmed G. Abo-Khalil, Synchronization of DFIG Output Voltage to Utility Grid in Wind Power System, Elsevier Journal of Renewable Energy, 44, 2012, pp. 193-198.
- [45] M.Q. Duong, S. Leva, M. Mussetta, K. H. Le, A Comparative Study on Controllers for Improving Transient Stability of DFIG Wind Turbines During Large Disturbances, Energies, Vol. 11, No. 480, 2018, pp. 1-18.
- [46] V. Yaramasu, B. Wu, P. C. Sen, S. Kouro, M. Narimani, High-power wind energy conversion systems: State-of-the-art and emerging technologies, Proc. IEEE, Vol. 103, 2015, pp.740–788.
- [47] A. G. Abo-Khalil, A. Alghamdi, I. Tlili, A. Eltamaly, Current Controller Design for DFIG-based Wind Turbines Using State Feedback Control, IET Renewable Power Generation, 2019.

## 7. Appendices

The specifications for the induction machine used for testing are as follows: three-phase, four poles, 230 [V], 50 [Hz], 3 [kW].

**Table 1.** Parameters of the Turbine Blade Model.

Parameters	Value
Blade radius	0.95 [m]
Max. power conv. coeff.	0.45
Optimal tip-speed ratio	7
Cut-in speed	4 [m/s]
Rated wind speed	13 [m/s]

**Table 2.** Parameters of the 3 kW Squirrel-Cage Induction Generator

Parameters	Value
Stator resistance	0.93 [ $\Omega$ ]
Rotor resistance	0.533 [ $\Omega$ ]
Iron loss resistance	190 [ $\Omega$ ]
Stator leakage inductance	0.003 [H]
Rotor leakage inductance	0.003 [H]
Mutual inductance	0.076 [H]